On the role of the flow permeability of metal foams on trailing edge noise reduction

Rubio Carpio, Alejandro; Avallone, Francesco; Ragni, Daniele

DOI
10.2514/6.2018-2964

Publication date
2018

Document Version
Final published version

Published in
2018 AIAA/CEAS Aeroacoustics Conference

AIAA AVIATION Forum
June 25-29, 2018, Atlanta, Georgia
2018 AIAA/CEAS Aeroacoustics Conference

10.2514/6.2018-2964

On the Role of the Flow Permeability of Metal Foams on Trailing Edge Noise Reduction

A. Rubio Carpio*, F. Avallone† and D. Ragni‡
Delft University of Technology, Delft, 2629 HS, The Netherlands

The turbulent flow over a NACA 0018 airfoil with porous trailing edge inserts and the resulting scattered turbulent-boundary-layer trailing edge noise are studied to investigate the effect of the cross-flow through the material. The experiments are performed at a chord-based Reynolds number of 2.63×10^5 and an angle of attack of 0°. Two different porous inserts, covering 20% of the chord, are manufactured with the same metal foam (cell diameter of 800 μm and permeability of 27×10^{-10} m^2). In order to assess the effect of the flow permeability on the far-field noise open and closed inserts are used. In the first ones the cellular structure is kept open, in the second ones the symmetry plane is filled with adherent material to impede flow communication between the two sides. The fully permeable trailing edge insert reduces noise intensity up to 11 dB for Strouhal number based on the chord lower than 16 while a noise increase is measured at higher frequencies. The non-permeable insert, on the other hand, does not show noise reduction with respect to the solid trailing edge below that Strouhal number but only noise increase at higher frequencies, confirming that flow permeability through the insert is necessary to achieve noise attenuation. The intensity of the noise increase is similar to that of the fully permeable insert thus suggesting that it is generated by the rough surface. The analysis of the mean flow field shows that only minor differences are present between the open and closed porous inserts. However, evidence of cross-flow through the material is found in the analysis of turbulent statistics.

I. Nomenclature

δ_{99}	=	Boundary layer thickness
δ_*	=	Displacement thickness
Φ_{uu}	=	Power spectral density of the wall-parallel/wall-normal
σ	=	Porosity
θ	=	Momentum thickness
c	=	Chord
c_0	=	Speed of sound
C	=	Drag factor
d_c	=	Cell diameter
f	=	Frequency
H	=	Shape factor
K	=	Permeability
L	=	Span
L_p	=	Sound Pressure Level
R	=	Resistivity
St	=	Chord-based Strouhal number
U_∞	=	Free-stream velocity
U_e	=	Edge velocity
u, v	=	Streamwise/vertical velocity fluctuations
U, V	=	Streamwise/vertical mean velocity
$\sqrt{\overline{u^2}}$	=	Root-mean-square of the streamwise velocity fluctuations

*Ph.D Student, AWEP Dept., a.rubiocarpio@tudelft.nl, AIAA Student Member
†Assistant Professor, AWEP Dept., f.avallone@@tudelft.nl
‡Assistant Professor, AWEP Dept., d.ragni@tudelft.nl

II. Introduction

Broadband trailing edge noise, produced by the scattering of turbulent flow at the airfoil trailing edge [1], represents the main source of noise in modern wind turbines [2]. In order to mitigate it, passive and active noise abatement techniques such as boundary layer injection/suction [3, 4], aeroacoustic optimization of the airfoil shape [5, 6], trailing edge serrations [7–9] or trailing edge brushes [10, 11] have been proposed. The installation of trailing edges manufactured with metal foam is an effective way to reduce noise [12], but the relationship between characteristics of the material (such as permeability and pore size) and the intensity of noise reduction has not yet been studied thoroughly.

The employment of porous materials to mitigate different aeroacoustic sound sources originating from trailing-edge flaps [13, 14], leading edges [15] and slat trailing edges [16] has been extensively investigated. Their application to trailing edge noise attenuation was first proposed in the 60s [17]. More recently, the research of Geyer et al. [18, 19] on fully porous airfoils showed up to 10 dB trailing edge noise reduction with respect to the baseline case. A wide range of porous materials, characterized by their resistivity R (analogous to the permeability), was tested in an attempt to link it to the scattered far-field noise; however, no simple connection between this property and the acoustic scattering was found. In spite of the noise attenuation benefits, fully porous airfoils showed a significant increase in drag and decrease in lift. To attenuate this, further experiments were performed with porous treatments restricted to the region of interest, i.e. the trailing edge [20]. Far-field noise abatement up to 8 dB was found even with a porous extent limited to 5% of the chord. With that configuration, only a 6% increase in drag was reported while the decrease in lift was negligible.

In order to understand how the properties of the porous treatments affect the scattered noise, further acoustic measurements on partially porous airfoils were carried out by Herr et al. [21]. Different permeable materials were tested on a DLRF16 airfoil trailing edge with a porous insert length equal to 10% of the chord. They reported noise reduction with respect to the solid case at lower frequencies (up to cross-over f = 10 kHz depending on the porous material) and noise increase above this frequency. High-frequency noise increase, previously attributed to a surface roughness contribution [19], was linked to the pore size. Larger noise abatement at low frequency was obtained using materials with higher permeability. Based on these results, a pressure release between suction and pressure sides was proposed as a necessary condition to achieve noise attenuation. However, due to the intrinsic difficulty of obtaining porous treatments with same pore characteristics but different flow permeability, such hypothesis was never confirmed.

In the present manuscript, noise scattered in presence of porous inserts manufactured with the same metal foam, yet distinct permeability is studied to assess the role of the latter on the far-field noise. Furthermore, the flow field around the inserts is also measured to evaluate if the noise attenuation is due to the scattering or to the variation of the hydrodynamic flow field. Measurements are carried out on a NACA 0018 airfoil at a chord-based Reynolds number of 2.63×10^5 and no incidence. Time-resolved Particle Image Velocimetry (PIV) is employed to acquire 2D-2C velocity fields at the midspan plane around the two different metal foam inserts, as well as a reference (solid) one. The metal foam is characterized in terms of permeability and pore size.

The manuscript is organized as follows. First, the measurement set-up, the metal foam characterization procedure and properties, the acoustic phased array and PIV arrangement, and the data reduction procedure are presented in section III. Then, far-field noise measurements, mean flow field, statistics and velocity spectra are discussed in section IV. Finally, in section V a summary of the main findings is reported.

III. Experimental Set-Up

A. Wind Tunnel Facility and Model

The experiments are performed in the anechoic vertical open-jet wind tunnel (A-Tunnel) at Delft University of Technology. The tunnel, with a rectangular test section of 40×70 cm^2, has a contraction ratio of 15:1 and can be operated at a free-stream velocity up to 45 m/s. The free-stream velocity distribution across the test section is uniform within 0.5% and the turbulence intensity is below 0.1% for the entire range of operative velocities. A NACA 0018 airfoil (Fig. 1 (a)), with chord c and span L lengths of 0.2 m and 0.4 m (span-to-chord ratio L/c = 2), is installed between two 1.2 m long side plates to guarantee two-dimensional flow (Fig. 2(a) and (b)). The airfoil, located 50 cm away from the contraction exit, is manufactured using Computer Numerical Control Machining (surface roughness: 0.05 mm) from a solid aluminium plate. Inter-changeable trailing edges are produced to allow for testing of different porous materials. The porous trailing edge inserts, manufactured using Electrical Discharge Machining, cover the last 20% (4 cm) of the chord (Fig. 1 (b)) to guarantee relevant changes in the flow field and acoustic emissions with respect to the solid case.

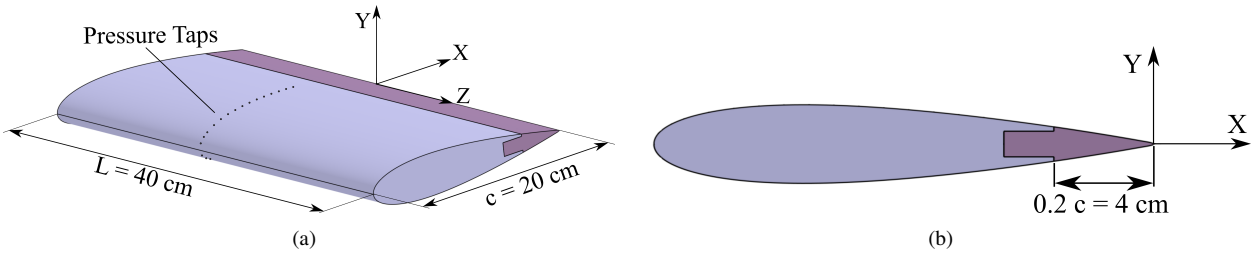

Fig. 1 Sketch of the NACA 0018 airfoil with porous insert. The aluminum body is represented in grey while the metal foam insert appears in purple. (a) General view. (b) Side view.

In order to assess the angle of attack α, static pressure measurements are obtained through 15 differential pressure *Honeywell* TruStability transducers (range: -0.6 to 0.6 kPa; accuracy: 3 Pa). Data are recorded at a sampling frequency of 100 Hz for 10 s. The pressure sensors are connected to 30 pressure orifices of 0.4 mm diameter, located within 1% and 66% of the chord, and equally distributed between the suction and the pressure sides. The orifices are tilted 15° with respect to the midspan plane of the airfoil ($Z = 0$) to avoid interference among themselves. The angle of attack is evaluated by comparing the measured static surface pressure distribution with the one given by the vortex-panel method XFOIL [22].

Turbulent boundary-layer transition is forced at 20% of the chord at both suction and pressure sides with carborundum particles of 0.84 mm diameter randomly distributed on a 10 mm tape strip. The broadband response of a remote microphone is employed to verify that the boundary-layer flow downstream the strip location is turbulent. The experiments are performed at a chord-based Reynolds numbers of 2.63×10^5, corresponding to a free-stream velocity $U_\infty = 20$ m/s, and an angle of attack of 0°.

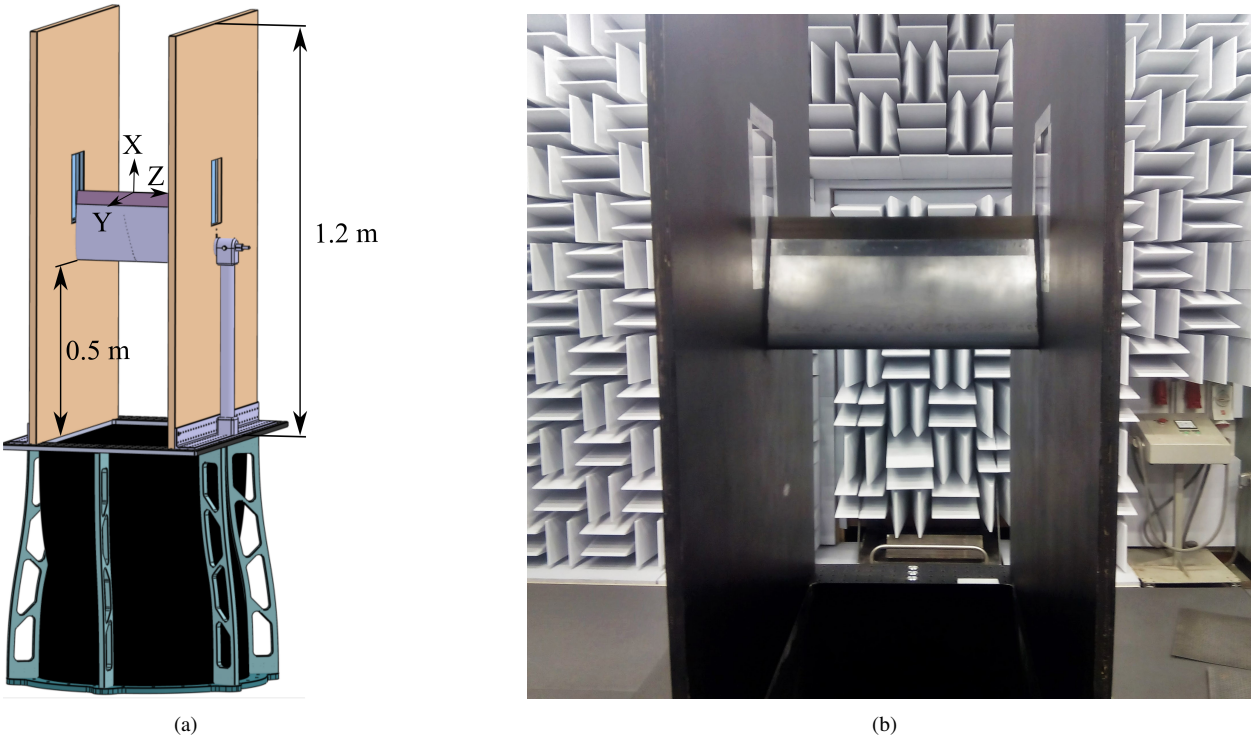

Fig. 2 Description of the test section. The flow direction is from bottom to top. (a) CAD including the contraction and the NACA 0018 airfoil installed between two side plates. (b) Closer view of the airfoil equipped with a porous insert.

B. Porous Inserts

The porous inserts are manufactured with an *Alantum* NiCrAl open-cell metal foam, obtained by electrodeposition of pure Ni on a polyurethane foam and subsequent coating with high-alloyed powder [23]. Its micro-structure consists of the three-dimensional repetition of a dodecahedron-shaped cell with nominal cell diameter d_c of 800 μm. Two different types of inserts are manufactured with this metal foam; the first one has an homogeneous distribution of the permeable material (Fig. 3 (a)), while a layer of *3M* EC-9323 B/A structural adhesive is applied in the symmetry plane of the second one to avoid cross-flow through the two sides (Fig. 3 (b)). For the sake of conciseness, these inserts are respectively referred as "permeable" and "non-permeable" in the manuscript.

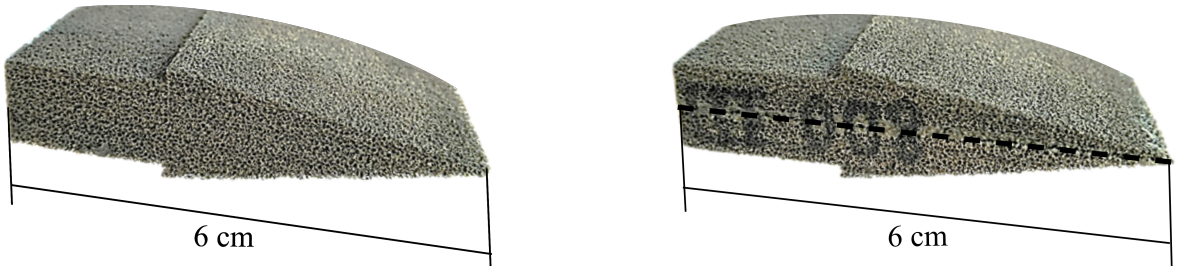

(a) (b)

Fig. 3 Metal foam inserts used in the experiments. (a) Permeable insert. (b) Non-permeable insert; the symmetry plane, where the adhesive layer is applied, is marked with a dashed line. The total length of the insert is 6 cm. Resolution: 10 px/mm.

1. Porosity

The porosity of the metal foam σ is defined as:

$$\sigma = 1 - \frac{\rho_p}{\rho_b} \tag{1}$$

where ρ_p and ρ_b are respectively the density of the foam and the base alloy (NiCrAl). The density of the porous foam ρ_p is calculated as the ratio between the weight and the volume of $10 \times 10 \times 5$ mm^3 samples. The samples are weighted using a *Mettler* Toledo AB204S analytical balance. In order to retrieve the density of the base alloy ρ_b, the approximate composition is obtained by energy-dispersive X-ray spectroscopy (EDS). The EDS analysis is carried out employing a *Jeol* JSM-7500F Field Emission Scanning Electron Microscope on the same samples used to calculate ρ_p. The measured values for the porosity are presented in table 1. It is verified that the porosity of the metal foam is 91.7%, in agreement with nominal data provided by the manufacturer (90%).

2. Permeability

The static pressure drop Δp across a homogeneous sample of permeable material with thickness t is described by the Hazen-Dupuit-Darcy equation [24]

$$\frac{\Delta p}{t} = \frac{\mu}{K} v_d + \rho C v_d^2 \tag{2}$$

where ρ is the fluid density, μ is the dynamic viscosity, v_d is the Darcian velocity (defined as the ratio between the volumetric flow rate and the cross-section area of the sample) and K and C are the permeability and the form coefficient, accounting for pressure loss due to viscous and inertial effects respectively. These two properties are obtained by least-squares fitting of Eq. (2) to 20 pressure drop data, measured for Darcian velocities ranging between 0 and 2.5 m/s.

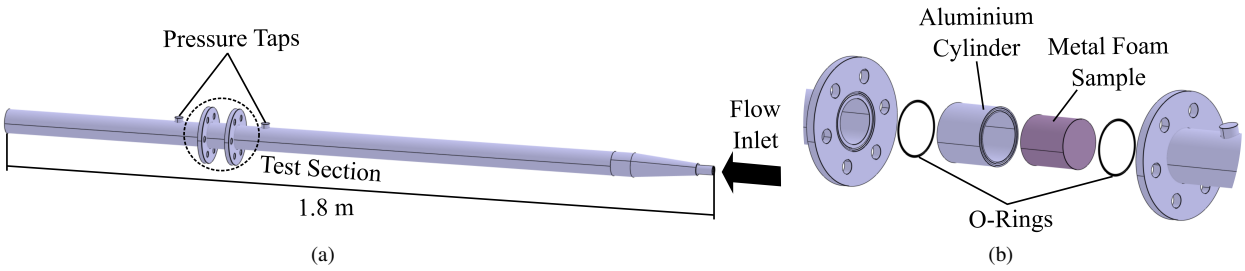

Fig. 4 (a) Sketch of the rig used to characterize the permeability/resistivity of the metal foams used during the experiments. (b) Detail of the test section.

The permeability measurements are carried out using the experimental rig shown in Fig. 4(a) and (b), specifically built for this purpose. The rig, supplied by air at 10 bar, allows to measure Δp between two pressure taps placed 5 cm upstream and downstream of the test section. The pressure taps are connected to a Mensor 2101 differential pressure sensor (range: -1.2 to 15 kPa; accuracy: 2 Pa). The volumetric flow rate is controlled using an *Aventics* pressure regulator and measured by a *TSI* 4040 volumetric flow meter (range: 0 to 2.5 m/s; accuracy: 2% of reading) located upstream the pipe.

The test section consists of an aluminum cylinder, into which 55 mm diameter metal foam disks are inserted. Previous studies [25, 26] showed that the permeability/drag coefficient measured on thin samples are biased due to the significance of entrance/exit effects on the measured pressure drop. To study the effect of the sample thickness, t, on K and C, samples with t ranging from 10 mm to 60 mm are tested. It is verified that the values of K and C obtained on foam samples with 50 and 60 mm thickness are approximately equal, i.e. entrance/exit effects are negligible. These values, reported in table 1, are in agreement with those published in previous literature [27, 28].

As stated in section II, the air flow resistivity $R = \Delta p/(t\ v_d)$ was employed to classify the porous treatments on previous research [29, 30]. This metal foam property, estimated in the present manuscript as $R = \mu/K$, is also reported in table 1 for comparison.

Table 1 Measured metal foam properties. Values in parenthesis refer to values provided by the manufacturer.

d_c (μm)	σ (%)	R (N·s/m^4)	K (m^2)	C (m^{-1})
(800)	91.7	6728	$27{\cdot}10^{-10}$	2613

C. Acoustic Phased Array Set-Up

Acoustic data are acquired using a 64-channel phased microphone array with *G.R.A.S.* 40PH free-field microphones (frequency response: ±1 dB; frequency range: 10 Hz to 20 kHz; max. output: 135 dB ref. $2{\cdot}10^{-5}$ Pa) and integrated CCP pre-amplifiers. The microphones are distributed (Fig. 5 (a)) within a modified Underbrink design [31], optimized to measure frequencies up to 10 kHz with minimum Main Lobe Width (MLW) and Maximum Sidelobe Level (MSL). The diameter of the array D is 2 m and the distance from the array plane to the airfoil trailing edge d is 1.48 m. The center of the array is aligned with the center of the airfoil trailing edge.

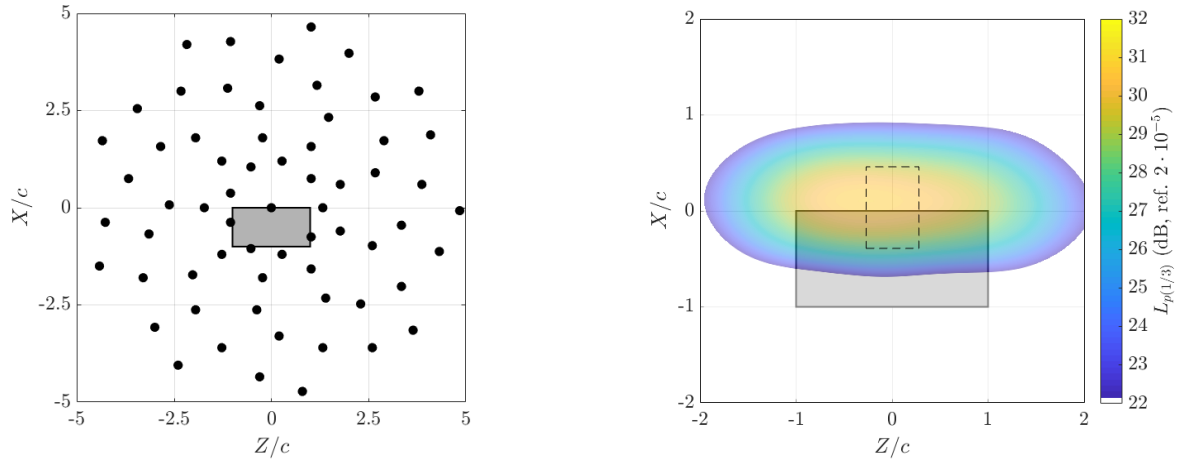

Fig. 5 (a) Distribution of phased microphones within the array. Coordinates are shown in the airfoil system X-Y-Z. The shaded area in grey represents the airfoil position with the flow direction in the positive X direction. (b) Source plot of the reference case for the 1/3 octave band with center frequency at f = 1.25 kHz. The projection of the airfoil in the X-Z plane is depicted. The integration area is represented as a dashed box.

Measurements are performed at a sampling frequency of 50 kHz during 60 s (3×10^6 samples). Acoustic data are separated in blocks of 8192 samples (Δt = 164 ms) for each Fourier transform and windowed using a Hann-weighting function with 50% overlap, thus providing a frequency resolution of about 6 Hz. The cross-spectral matrix (CSM) of the measured acoustic pressure is obtained by averaging the Fourier-transformed sample blocks over time. In previous studies [32] with a similar experimental set-up, the source power was retrieved within an accuracy of 1 dB. Beamforming is performed on a square grid ranging between -2 < X/c < 2 and -2 < Z/c < 2 and distance between grid points of 1 cm. The minimum distance at which the array can resolve two sources R_c is given by the Rayleigh criterion [33, 34] as $R_c \simeq d \tan(1.22\, c_0/(f\, D))$, where c_0 refers to the speed of sound. For the highest measured frequency shown in the present investigation (f = 3 kHz), the minimum distance is R_c =10 cm. Hence, the space between grid points is 10 times smaller than the maximum resolution of the array. Conventional frequency domain beamforming [35] is applied to the acoustic data. Due to the characteristics of the experimental setup, the minimum frequency measured with sufficient resolution and signal-to-noise ratio for the acoustic spectra is 500 Hz. Integration of the source map in the range -0.27 < Z/c < 0.27 and -0.39 < X/c < 0.46 (dashed box in Fig. 5 (b)) is performed [36] to retrieve noise generated at the trailing edge minimizing the effect of neighboring noise sources. This method has provided with satisfactory results for trailing edge noise data obtained through simulations [37] and experiments [38, 39].

D. High Speed Particle Image Velocimetry

Two-dimensional velocity fields at the suction and pressure sides are synchronously acquired by means of planar PIV, performed at the midspan plane (X-Y) of the airfoil. The experimental set-up is depicted in Fig. 6(a).

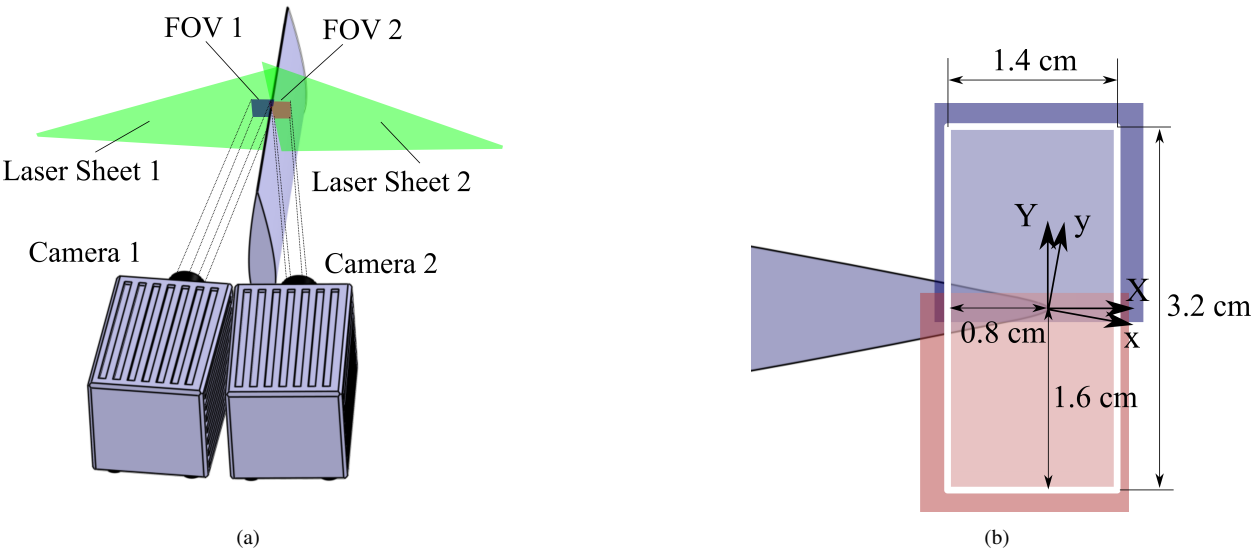

(a) (b)

Fig. 6 (a) Sketch of the PIV set-up. (b) Detail of the FOV and coordinate system. The original FOV of the cameras are represented by the green and red areas. The final FOV, obtained after joining and cropping them, is marked with the white shadowed area.

Seeding is produced by a *SAFEX* Twin-Fog Double Power fog generator using a glycol-based solution (mean droplet diameter: 1 μm). Illumination is provided by laser pulses generated by a *Continuum* MESA PIV 532-120-M Nd:YAG system (laser wavelength: 532 nm; energy: 18 mJ/pulse). Two laser sheets from the same illumination source are obtained using a beam splitter; laser optics are employed to turn the beams into laser sheets of approximately 1 mm thickness conveniently aligned into the same plane.

Images are recorded using 2 *Photron* Fastcam SA-1 CMOS cameras (1024×1024 pixel^2, 12 bit, pixel size 20 μm), placed at 25 cm from the measurement plane. The cameras are equipped with *Nikon* NIKKOR 200 mm focal distance macro-objective set to aperture $f_\# = 4$. In order to minimize peak-locking, the plane of focus is offset with respect to the laser sheet, as suggested in Raffel et al. [40], so that the particle image is larger than 2 px. The image acquisition and the illumination are triggered synchronously using a *LaVision* high speed controller. Time-resolved data is acquired at a sampling frequency of 20 kHz (21829 images). The sensor of the camera is cropped to 512×512 pixels. The field of view (FOV) of each camera is of $0.1c$×$0.1c$ (20×20 mm^2) with a digital resolution of approximately 25 px/mm. Calibration and combination of the single fields of view is shown in Fig. 6(b) with a final FOV of $0.16c$×$0.07c$ (32×14 mm^2). The measured area is limited to -0.04 $\leq X/c \leq$ 0.03 in the stream-wise direction and -0.08 $\leq Y/c \leq$ 0.08 in the vertical direction.

The images are processed using *LaVision* DaVis 8.4 software. A multi-pass cross-correlation algorithm [41] with window deformation [42] is applied to the sequence of images resulting in an ensemble of 21828 vector fields. The final interrogation window size is 24×24 pixel^2 with an overlap factor of 75%g, yielding a final spatial resolution of 0.94 mm and a vector spacing of 0.24 mm. Approximately 0.8% of the vectors is classified as spurious with the universal outlier detector [43]; consequently, they are replaced by linear interpolation based on adjacent data. The main characteristics of the camera and the acquisition parameters are summarized in table 2.

Two coordinate systems, also plotted in Fig. 6(b), are used in the present manuscript. Both coordinate systems have the origin at the intersection between the trailing edge and the midspan plane of the airfoil. The X-Y-Z system, used to describe wake flow, has the X and Z-axis aligned with the chord and the trailing edge of the airfoil. The x-y-z coordinate system, used for boundary layer flow analysis, is rotated with respect to the previously defined stream-wise vertical plane $X - Y$ so that the x and y directions are parallel and normal to the surface of the trailing edge insert, respectively.

Table 2 PIV acquisition parameters

Parameter	Quantity
Cameras	*Photron* Fastcam SA1.1
Acquisition frequency	20 kHz
Acquisition sensor	512×512 px^2
Single FOV	20×20 mm^2
Total FOV	32×14 mm^2
Digital resolution	25 px/mm
Magnification factor	0.51
Interrogation window	24×24 px^2
Overlap factor	75%
Vectors per velocity field	136×60
Vector spacing	0.24×0.24 mm^2
Free-stream pixel displacement	20 px

1. Data Reduction and Processing

The mean and turbulent flow fields are obtained by down-sampling the correlated dataset with a frequency f_{us} = 500 Hz, thus yielding a data-set of 546 PIV snapshots. The down-sampling frequency is chosen by analyzing the auto-correlation function of the wall-parallel u velocity fluctuations at the point of maximum turbulence intensity (x/c = 0, y/δ_{99} = 0.5) over the solid insert. Convergence of the mean and statistic flow quantities within the reduced data-set has been assessed.

The correlated data-set is band-pass filtered with cut-off frequencies equal to 50 Hz and 10 kHz. The analysis of this data-set in the frequency domain is performed using the power spectral density of the wall-parallel velocity fluctuations Φ_{uu}. This quantity is obtained throughout the Welch's method [44]: signals are divided in time blocks of 512 samples (25 ms) with 50 % overlapping and windowed using the Hann function; the frequency resolution is thus 39 Hz.

2. Uncertainty Analysis

The estimation of PIV uncertainty is carried out quantifying the random and bias errors. The random error considers the cross-correlation error, which is 0.1 pixel (0.4% of U_∞) [45], and the effect of turbulence on the convergence of statistic quantities.

The systematic errors include peak-locking, particle slip, inaccurate image superposition and calibration errors. The error due to peak-locking, quantified with the cumulative sum of the decimal particle displacement, is found to be always around 0.05 pixel (0.2% of U_∞). The inaccuracy due to the combination of velocity fields to obtain the complete FOV is estimated at 1 pixel (4% of U_∞). The particle slip [46], caused by the lag between tracer and flow, is calculated as $U_{slip} = \tau_{slip} \cdot a_p$, where the particle acceleration a_p is obtained through the material derivative of the velocity field. The response time associated to the tracer particle (τ_{slip} = 0.5 μs) is satisfactory for the average particle acceleration found in the boundary layer (3800 m/s^2), yielding a final U_{slip} equal to 0.01% of U_∞. Spatial calibration of the camera is applied using a two-dimensional known target, with a positioning error of ±0.5 mm. To account for any optical distortion, images are mapped using a third order polynomial fit which allows mapping of the physical space into the sensor one. The accuracy of the fit is 0.8 pixel, corresponding to an uncertainty of 3% of U_∞.

Using a linear propagation approach [47], the uncertainty on the mean and root-mean-square (r.m.s.) velocity have respectively upper bound values of $0.03U_\infty$ and $0.04\sqrt{\overline{u^2}}$, found at the point of maximum intensity of the velocity fluctuations (defined above). These values are verified using the error quantification method introduced by Wieneke [48]. The latter gives an uncertainty on the mean quantities of $0.02U_\infty$ and on the r.m.s. quantities of $0.03\sqrt{\overline{u^2}}$, considering a 95% confidence interval.

IV. Results

A. Far-field Noise

Trailing edge noise measurements for both metal foam inserts as well as the baseline case are presented in Fig. 7(a) in Sound Pressure Level L_p in dB relative to a reference pressure of $p_{ref} = 20\ \mu Pa$. The L_p values, calculated as $L_p = 10\log_{10}\left(\overline{p^2}/p_{ref}^2\right)$ are expressed as a function of the chord-based Strouhal number $St = fc/U_\infty$. The relative L_p with respect to the baseline case, calculated as $\Delta L_p = L_p^{solid} - L_p^{porous}$, is also reported in Fig. 7(b). As expected, the permeable insert shows up to 11 dB noise attenuation with respect to the solid insert below cross-over $St = 16$, with maximum noise abatement being measured at $St = 5.5$. Conversely, up to 9 dB excess noise is reported above this cross-over St; as explained in section II, this high-frequency increase has been previously attributed to a surface roughness contribution [18, 30]. Interestingly, there are no significant differences between the solid and the non-permeable foam insert below the cross-over St; this confirms that suction and pressure sides must communicate to achieve noise abatement, as suggested in Herr et al. [21]. In addition, this finding also corroborates that, at least for this type of material, the sound absorbing properties of the foam are not relevant for trailing edge noise attenuation. Further analysis of the non-permeable insert reveals that above the cross-over St it produces comparable L_p levels to the permeable insert (with a maximum difference of 2.5 dB at $St = 21$); the fact that both spectra have similar slope within this frequency range suggests that are produced by the same phenomenon, i.e. surface roughness.

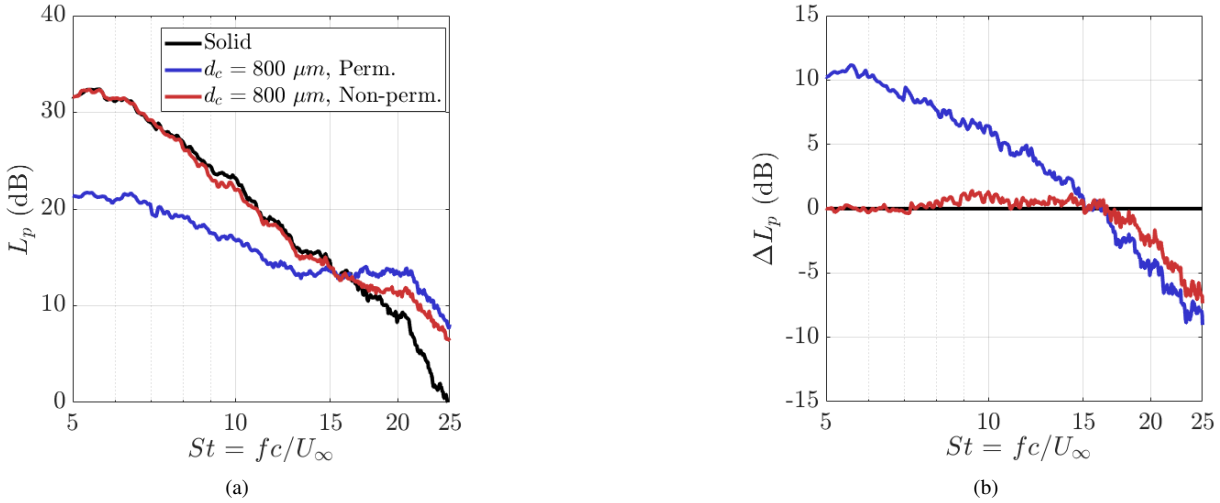

Fig. 7 Sound Pressure Level L_p for the solid and metal foam inserts. The acoustic energy corresponds to a 6 Hz band. These values correspond to an observer placed at the center of the array. (a) Absolute values. (b) Relative values with respect to the solid case.

B. Flow Field

The flow field measured around the three inserts is described in this section in order to assess whether changes in the flow field induced by the characteristics of the material support the previously described acoustic scattering. Firstly, data measured for the baseline case are compared to previous experimental data measured on analogous conditions [9, 36] and XFOIL [22] to validate the present results.

Table 3 Comparison of boundary layer thickness δ_{99}, displacement thickness δ_*, momentum thickness θ and shape factor H values measured at the trailing edge in the present investigation with values presented in previous studies and XFOIL.

Investigation	δ_{99} (mm)	δ_* (mm)	θ (mm)	H
Present	9.1	3.4	1.5	2.3
Arce León et al. [36]	9.4	2.1	1.3	1.6
Avallone et al. [9]	9.5	3.3	1.5	2.2
XFOIL [22]	-	2.3	1.2	2

In table 3, displacement thickness δ_* and momentum thickness θ values measured at the trailing edge ($X/c = 0$) are presented. In the present study, the aforementioned boundary layer integral quantities are calculated following the procedure proposed by Spalart and Watmuff [49], i.e., the boundary layer edge is evaluated as the point where the integral of the vorticity along the wall-normal direction converges to a steady value. The boundary layer thickness δ_{99}, defined as the point where the wall-parallel velocity is 99% of the edge velocity U_e, and the shape factor $H = \delta_*/\theta$ are also reported for the sake of completeness. The boundary layer parameters obtained in the present experiment show a good overall agreement with values reported in previous studies; the apparent lack of agreement in δ_* can be attributed to distinct tripping devices. As shown in Fig. 8, similar values are found on suction and pressure sides of the solid insert, giving further validation to the angle of attack set during the experiment.

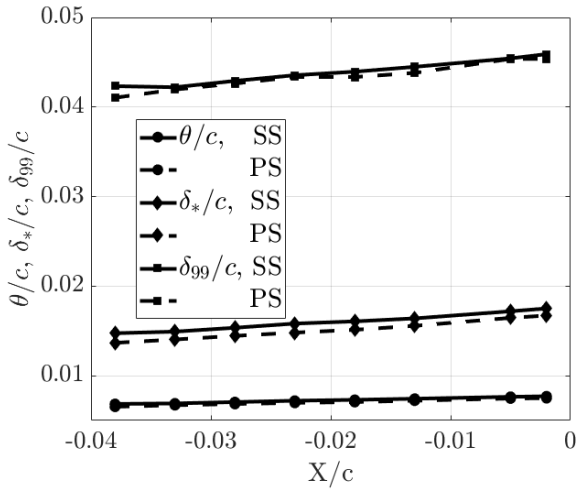

Fig. 8 Boundary layer thickness δ_{99}/c, displacement thickness δ_*/c and momentum thickness θ/c at the suction and pressure sides of the solid insert.

Mean streamwise U/U_∞ and vertical V/U_∞ velocity fields around the solid, permeable and non-permeable foam inserts are respectively plotted in Fig.9(a-f) together with their streamlines. It is observed that, despite having diverse properties, the type of insert have limited effects on the mean flow field. It is also interesting to note that the steady cross-flow from pressure side to suction side of permeable inserts, described in experiments/simulations with airfoils at incidence [50], is not present here due to the lack of significant pressure imbalance between both sides.

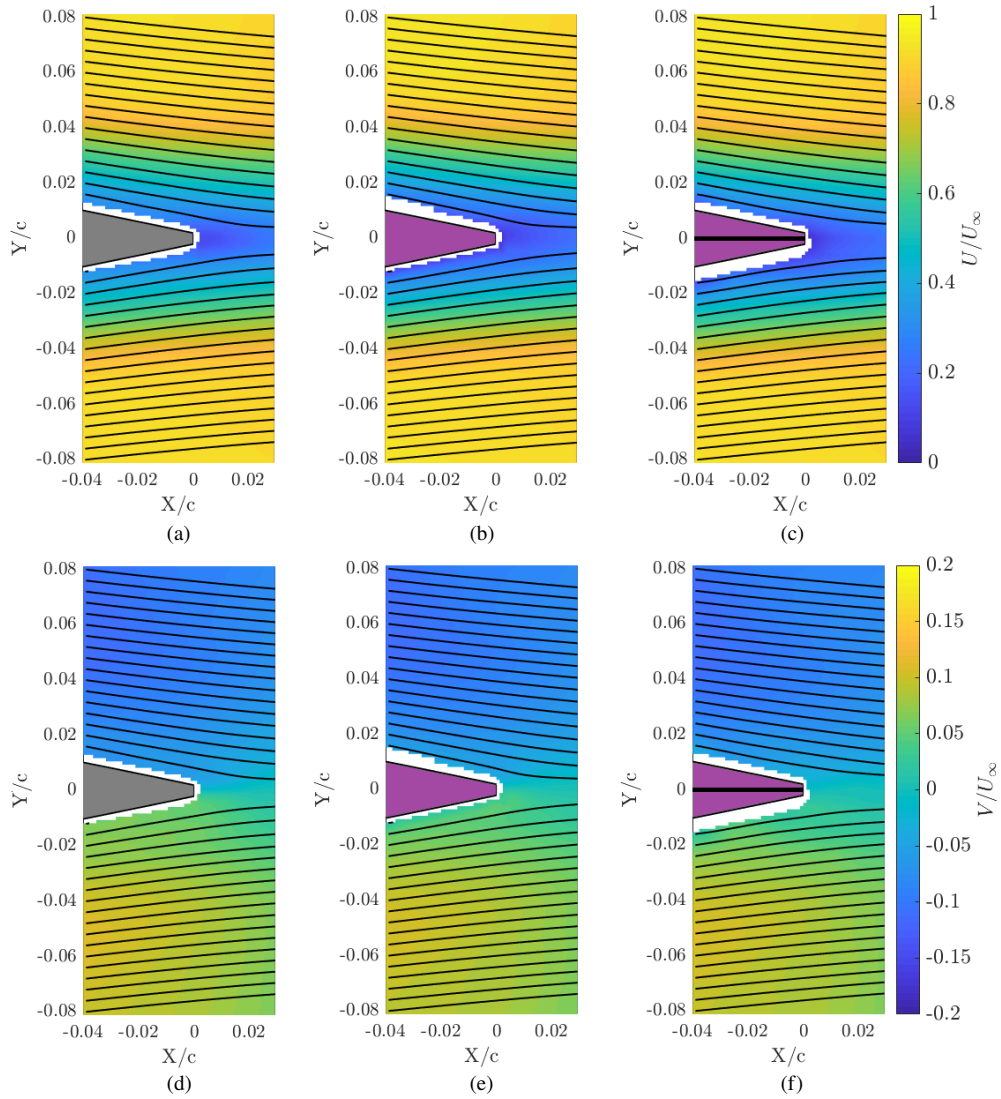

Fig. 9 Mean streamwise U/U_∞ (a-c) and vertical V/U_∞ (d-f) velocity fields for the solid (a, d), permeable metal foam (b, e) and non-permeable metal foam inserts (c, f). The streamlines start at X/c = -0.04 and are initially separated 0.8 mm (0.004c) in the vertical direction Y.

A more detailed comparison of mean flow field quantities for the three inserts is presented in Fig. 10(a), (b) and (c). Profiles of the wall-parallel velocity U measured at the trailing edge ($X/c = 0$) are shown in Fig. 10(b); the wall-normal axis y and U are respectively normalized by δ_{99} and U_∞. The coordinates of the wall-normal profile are marked in Fig. 10(a) with a dashed line. Decrease of the mean wall-parallel velocity with respect to the baseline insert, i.e. a velocity deficit, arises for wall-normal positions $y/\delta_{99} \leq 0.5$ for the metal foam inserts. The velocity deficit was also reported in previous experiments with porous trailing edge inserts [20] and it is commonly found for rough surfaces [51, 52] due to their higher surface drag. In Fig. 10(c), profiles of the streamwise velocity U at $X/c = 0.02$ are plotted. The coordinates where the vertical profile is measured are also highlighted in Fig. 10(a) by the dotted line. Results show that porous treatments do not have a significant effect on the wake flow; although the wake velocity deficit is larger for the porous treatments, differences with respect to the solid case are small: up to $0.02U_\infty$ reduction for the permeable insert and up to $0.01U_\infty$ for the non-permeable insert at the chord-line $Y/c = 0$. In spite of its magnitude, such a change of the wake flow suggests a reduced form drag with respect to the baseline case. However, an increase of the overall drag has been reported in previous literature on airfoils with porous inserts [21, 29]. This apparently contradictory result might be explained by the increase of friction drag associated to rough surfaces [53].

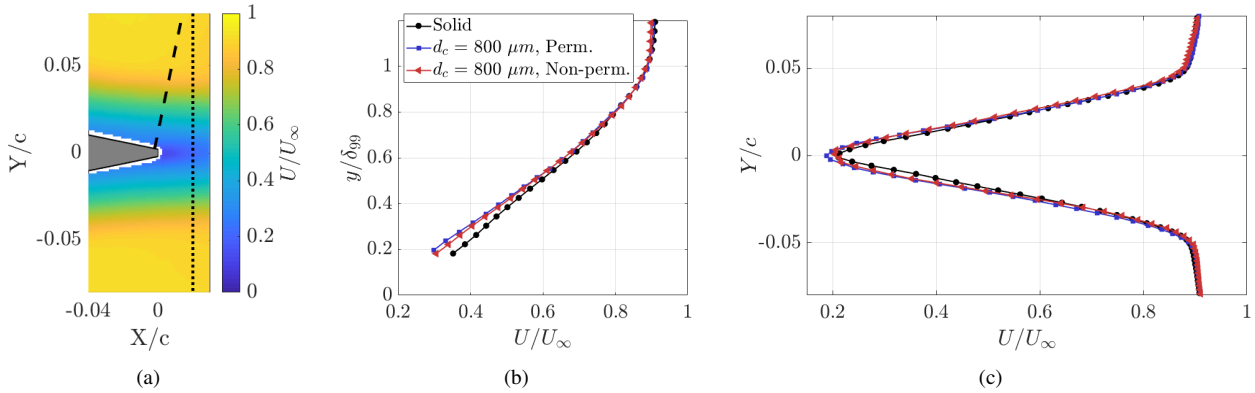

Fig. 10 Mean velocity profiles at the trailing edge and downstream ($X/c = 0.02$) for the three inserts. (a) Streamwise velocity field U pointing out the location where velocity is measured. Dashed line: $X/c = 0$. Dotted line: $X/c = 0.02$. (b) Mean wall-parallel velocity profile at $X/c = 0$. (c) Mean streamwise velocity profile at $X/c = 0.02$.

To conclude the analysis of the mean flow field, the variation of δ_{99}, δ_* and θ with streamwise positions X for the three inserts are compared in Fig. 11(a), (b) and (c). It can be seen that these boundary layer quantities are similar for both metal foam inserts, and larger than those of the reference case. The increase of δ_* and θ with respect to the solid edge can be attributed to the velocity deficit described before. Interestingly, these quantities are relevant for trailing edge noise scattered by solid edges [54]; however, given the very different acoustic scattering it is obvious that they are not driving the noise generation, as suggested in [29]. Increase of these boundary layer quantities was previously attributed to a higher permeability of the employed porous treatment [19]; in contrast with this hypothesis, the present results show that the change of boundary layer topology is mainly due to roughness effects, and it should be linked to the pore size rather than to the permeability.

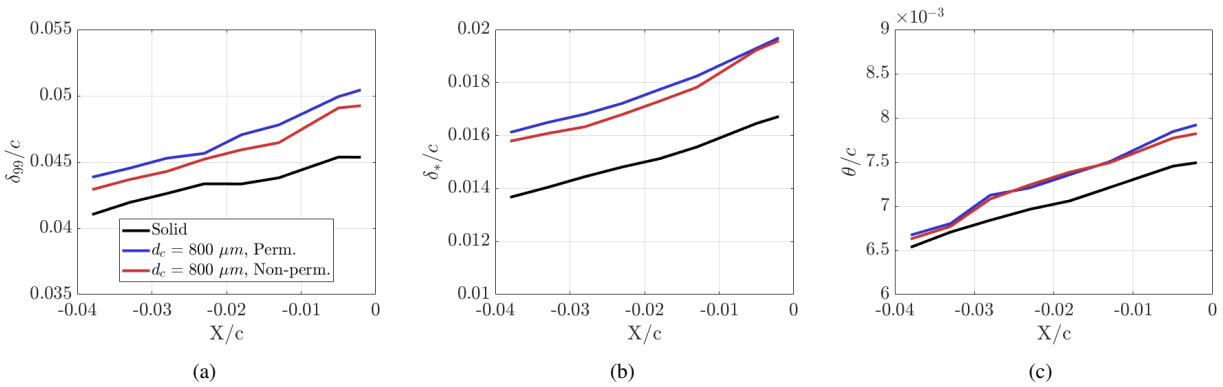

Fig. 11 Boundary layer topology parameters for the three measured inserts. (a) Boundary layer thickness δ_{99}/c (b) Displacement thickness δ_*/c (c) Momentum thickness θ/c

To assess the effect of porous treatments on the turbulence statistics, profiles of the wall-parallel r.m.s. velocity $\sqrt{\overline{u^2}}$ and Reynolds stress $-\overline{uv}$ at the trailing edge ($X/c = 0$) are presented in Fig. 12(a) and (b). It is observed that permeable and non-permeable treatments have opposite effects on these quantities: while the non-permeable insert produces an overall decrease with respect to the solid case within a large part of the boundary layer ($y/\delta_{99} \leq 0.8$), the permeable insert shows an increase ($y/\delta_{99} \leq 0.6$). Although not shown here, the analysis of $\sqrt{\overline{v^2}}$ yields similar conclusions. Increase of turbulence intensity within the near-wall boundary layer region due to permeable metal foams was also found in Showkat Ali et al. [55] on experiments on a plate with a permeable extension. In that case, such an increase was attributed to the growth of frictional forces acting along the rough surface. However, this hypothesis cannot explain the present results. Given the facts that the only significant difference between both porous inserts regards the

permeability, and that the rise of $\sqrt{\overline{u^2}}$ and $-\overline{uv}$ in the permeable case takes place exclusively close to the wall, a likely explanation for the increase of turbulent statistics is the appearance of unsteady cross-flow through the foam. This cross-flow might be the reason of the different acoustic scattering reported in section A: it would communicate turbulent fluctuations from suction and pressure sides, thus modifying the acoustic impedance discontinuity at the edge.

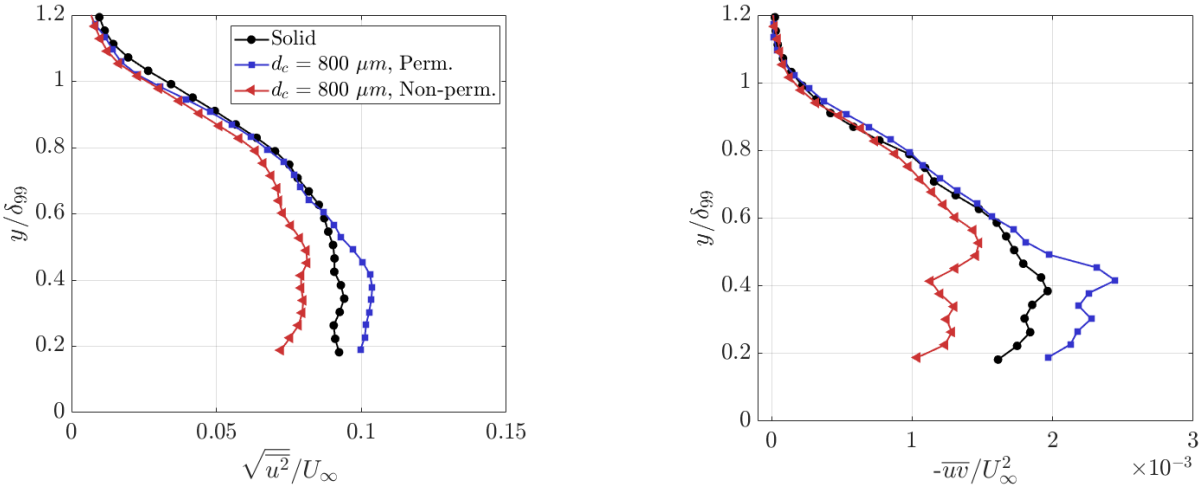

Fig. 12 Turbulence quantities for the three measured inserts at X/c = 0. (a) Profile of the wall-parallel r.m.s. velocity $\sqrt{\overline{u^2}}/U_\infty$. (b) Profile of the Reynolds stress $-\overline{uv}/U_\infty^2$.

Further analysis of the spectral content of wall-parallel velocity fluctuations is presented in Fig. 13 in terms of the power spectral density Φ_{uu}. These values are measured at $y/\delta_{99} = 0.3$ above the trailing edge. It is observed that the spectra follow the Kolmogorov's decay law [56] properly up to $St = 50$, above which they are flattened. This behavior is due to the limited temporal resolution of PIV; it has been previously reported [57] that the frequency analysis of the measured signals should be narrowed up to 3/4 of the Nyquist frequency ($St = 75$). Deviation from the Kolmogorov decay at a lower St is due to the lower signal-to-noise ratio, caused by the presence of laser reflections. The analysis of Φ_{uu} shows that the increase of the energy of the fluctuations due to the permeable insert is confined below $St = 15$ with a maximum difference of 3 dB at $St = 3$, in agreement with acoustic cross-over St and the location of the maximum noise reduction reported in section A. This supports the cross-flow as a significant contributor to noise abatement. On the other hand, the non-permeable insert produces a decrease of the fluctuations below $St = 22$, in agreement with results shown in Fig. 12(a). No evidence of increase of the energy of fluctuations above $St = 15$, which would explain surface roughness noise contribution is found.

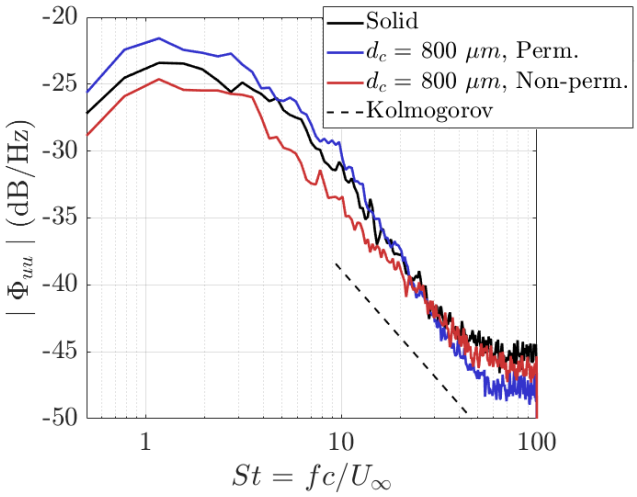

Fig. 13 Power spectral density of the wall-parallel Φ_{uu} velocity fluctuations at (X/c = -0.002, y/δ_{99}=0.3)

Finally, profiles of $\sqrt{\overline{u^2}}/U_\infty$ and $-\overline{uv}/U_\infty^2$ within the wake ($X/c = 0.02$) are respectively shown in Fig. 14(a) and (b) for the three inserts. It is observed that profiles of the aforementioned quantities are symmetric with respect to the chord-line ($Y/c = 0$) and have their maximum around $Y/c = 0.015$. Results show that the permeable insert increases $\sqrt{\overline{u^2}}/U_\infty$ and $-\overline{uv}/U_\infty^2$ with respect to the reference case; conversely, the non-permeable insert leads to decreased turbulent motions $-\overline{uv}/U_\infty^2$, in agreement with the analysis of these quantities above the trailing edge.

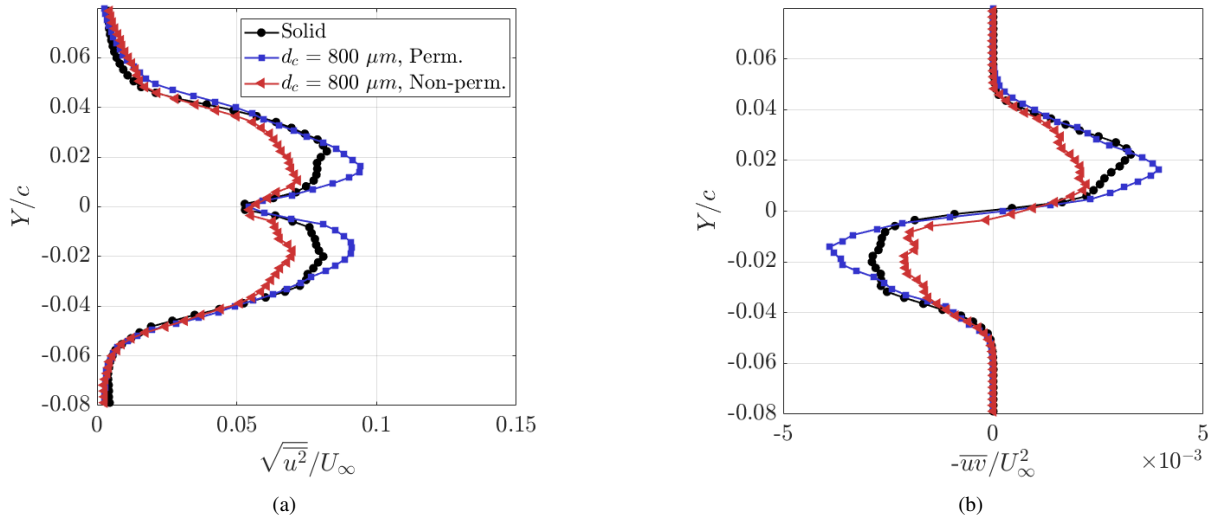

(a) (b)

Fig. 14 Turbulence quantities for the three measured inserts at X/c = 0.02. (a) Profile of the wall-parallel r.m.s. velocity $\sqrt{\overline{u^2}}/U_\infty$. (b) Profile of the Reynolds stress $-\overline{uv}/U_\infty^2$.

V. Conclusions

Aerodynamic and acoustic measurements on a NACA 0018 airfoil with solid and porous trailing edge inserts covering 20% of the chord length are performed. Two porous inserts are manufactured with the same type of metal foam. A non-permeable membrane is applied in the symmetry plane of one of the inserts to avoid cross-flow between the sides of the airfoil through the foam.

Far-field noise results, measured with a phased microphone array, show up to 11 dB noise attenuation with respect

to the solid insert below cross-over $St = 16$ only for the permeable insert, with maximum noise abatement being measured at $St = 5.5$. Conversely, non-permeable metal foam and solid inserts produce similar far-field noise below the cross-over St. These findings confirm that flow communication between suction and pressure sides through the foam is a necessary condition to achieve noise abatement with respect to the baseline case. They also prove that the acoustically absorbent properties of the foam used in the present investigation are not relevant for noise attenuation purposes. The fact that permeable and non-permeable metal foam inserts produce very similar excess noise above the cross-over St also supports the roughness of the treatment as the origin of this contribution.

Time-resolved planar PIV measurements are performed to study the flow field around the inserts. Mean flow field analysis shows that porous inserts do not affect significantly the mean flow field in absence of incidence. Conversely, relevant effects on the boundary layer topology are reported: increase of the boundary layer thickness, displacement thickness and momentum thickness with respect to the baseline case is measured for both porous treatments. It is also assessed that these modifications have their origin on the higher roughness of the treatments. On the basis of the very different acoustic scattering produced by porous treatments with similar boundary layer topology, it is concluded that these quantities are not relevant for porous trailing edge noise production, in contrast to noise generation for solid edges. No significant changes of the wake topology or velocity magnitude are reported. The Reynolds stress analysis suggests the presence of cross-flow through the foam insert only for the permeable case. It is proposed that this flow might be responsible of decreasing the acoustic impedance of the edge, thus providing an explanation for the reported differences in the acoustic scattering of the treatments. The presence of the cross-flow through the permeable insert is supported by the analysis of the velocity fluctuations in the frequency domain, which shows an increase of their energy intensity with respect to the baseline case below $St = 15$, in agreement with the previously reported acoustic cross-over St. No evidence of an increase of high-frequency fluctuations, that could support reported high frequency excess noise is measured for the porous treatments.

The previously described changes in the boundary layer or the wake of the airfoil do not fully explain reported changes in acoustic scattering of porous edges. Thus, further analysis to shed light on the causes of trailing edge noise reduction using permeable treatments, such as the modification of the acoustic impedance of the edge or the reduction in spanwise coherence of the wall-pressure fluctuations, will be subject to study in the future.

References

[1] Brooks, T. F., Pope, D. S., and Marcolini, M. A., "Airfoil Self-Noise and Prediction," *NASA Reference Publication*, 1989.

[2] Oerlemans, S., Sijtsma, P., and Lopez, B. M., "Location And Quantification Of Noise Sources On A Wind Turbine." *Journal of Sound and Vibration*, 2007. doi:10.1016/j.jsv.2006.07.032.

[3] Szoke, M., and Azarpeyvand, M., "Active Flow Control Methods for the Reduction of Trailing Edge Noise," *23rd AIAA/CEAS Aeroacoustics Conference*, American Institute of Aeronautics and Astronautics, 2017. doi:10.2514/6.2017-3004.

[4] Arnold, B., Rautmann, C., Lutz, T., and Kraemer, E., "Design of a Boundary-Layer Suction System for Trailing-Edge Noise Reduction of an Industrial Wind Turbine," *35th Wind Energy Symposium*, American Institute of Aeronautics and Astronautics, 2017. doi:10.2514/6.2017-1380.

[5] Mardsen, A. L., Wang, M., Dennis, J. E., and Moin., P., "Trailing Edge Noise Reduction Using Derivative-free Optimization And Large Eddy Simulation," *Journal of Fluid Mechanics*, 2007. doi:10.1017/S0022112006003235.

[6] Oerlemans, S., Fisher, M., Maeder, T., and Kogler, K., "Reduction of Wind Turbine Noise Using Optimized Airfoils and Trailing-Edge Serrations," *AIAA Journal*, Vol. 47, No. 6, 2009, pp. 1470–1481. doi:10.2514/1.38888.

[7] Moreau, D. J., and Doolan, C. J., "Noise-Reduction Mechanism of a Flat-Plate Serrated Trailing Edge," *AIAA Journal*, Vol. 51, No. 10, 2013, pp. 2513–2522. doi:10.2514/1.j052436.

[8] Arce León, C., Ragni, D., Probsting, S., Scarano, F., and Madsen, J., "Flow Topology And Acoustic Emissions Of Trailing Edge Serrations At Incidence," *Experiments in Fluids*, 2016. doi:10.1007/s00348-016-2181-1.

[9] Avallone, F., Probsting, S., and Ragni, D., "Three-dimensional flow field over a trailing-edge serration and implications on broadband noise," *Physics of Fluids*, Vol. 28, No. 11, 2016, p. 117101. doi:10.1063/1.4966633.

[10] Herr, M., and Dobrzynski, W., "Experimental Investigations in Low-Noise Trailing Edge Design," *AIAA Journal*, Vol. 43, No. 6, 2005, pp. 1167–1175. doi:10.2514/1.11101.

[11] Finez, A., Jacob, M., Jondeau, E., and Roger, M., "Broadband Noise Reduction with Trailing Edge Brushes," *16th AIAA/CEAS Aeroacoustics Conference*, American Institute of Aeronautics and Astronautics, 2010. doi:10.2514/6.2010-3980.

[12] Rubio Carpio, A., R., M. M., Avallone, F., Ragni, D., Snellen, M., and van der Zwaag, S., "Broadband Trailing Edge Noise Reduction Using Permeable Metal Foams." *46th International Congress and Exposition on Noise Control Engineering*, 2017, pp. 1–11.

[13] Fink, M., and Bailey, D., "Model tests of airframe noise reduction concepts," *6th Aeroacoustics Conference*, American Institute of Aeronautics and Astronautics, 1980. doi:10.2514/6.1980-979.

[14] Revell, J., Kuntz, H., Balena, F., Horne, C., Storms, B., and Dougherty, R., "Trailing-edge flap noise reduction by porous acoustic treatment," *3rd AIAA/CEAS Aeroacoustics Conference*, American Institute of Aeronautics and Astronautics, 1997. doi:10.2514/6.1997-1646.

[15] Lee, S., "Reduction of blade-vortex interaction noise through porous leading edge," *AIAA Journal*, Vol. 32, No. 3, 1994, pp. 480–488. doi:10.2514/3.12011.

[16] Khorrami, M. R., and Choudhari, M. M., "Application of Passive Porous Treatment to Slat Trailing Edge Noise," *NASA Technical Report 762-20-11-04*, 2003.

[17] Lowson, M. V., "Reduction of Compressor Noise Radiation," *The Journal of the Acoustical Society of America*, Vol. 43, No. 1, 1968, pp. 37–50. doi:10.1121/1.1910760.

[18] Geyer, T., and Sarradj, E., "Noise Generation by Porous Airfoils." *13th AIAA/CEAS Aeroacoustics Conference*, 2007.

[19] Geyer, T., Sarradj, E., and Fritzsche, C., "Porous Airfoils: Noise Reduction and Boundary Layer Effects," *International Journal of Aeroacoustics*, Vol. 9, No. 6, 2010, pp. 787–820. doi:10.1260/1475-472x.9.6.787.

[20] Geyer, T., and Sarradj, E., "Trailing Edge Noise of Partially Porous Airfoils," *20th AIAA/CEAS Aeroacoustics Conference*, 2014. doi:10.2514/6.2014-3039.

[21] Herr, M., Rossignol, K. S., Delfs, J., Lippitz, N., and Moßner, M., "Specification of Porous Materials for Low-Noise Trailing-Edge Applications," *20th AIAA/CEAS Aeroacoustics Conference*, American Institute of Aeronautics and Astronautics (AIAA), 2014. doi:10.2514/6.2014-3041.

[22] Drela, M., *XFOIL: An Analysis and Design System for Low Reynolds Number Airfoils*, Springer Berlin Heidelberg, Berlin, Heidelberg, 1989, pp. 1–12. doi:10.1007/978-3-642-84010-4_1.

[23] Kim, S., and Lee, C., "A Review on Manufacturing and Application of Open-cell Metal Foam," *Procedia Materials Science*, Vol. 4, 2014, pp. 305–309. doi:10.1016/j.mspro.2014.07.562.

[24] D.Ingham, and Pop, I., *Transport Phenomena in Porous Media*, Pergamon, 1998.

[25] Baril, E., Mostafid, A., Lefebvre, L.-P., and Medraj, M., "Experimental Demonstration of Entrance/Exit Effects on the Permeability Measurements of Porous Materials," *Advanced Engineering Materials*, Vol. 10, No. 9, 2008, pp. 889–894. doi:10.1002/adem.200800142.

[26] Dukhan, N., and Patel, K., "Effect of sample's length on flow properties of open-cell metal foam and pressure-drop correlations," *Journal of Porous Materials*, Vol. 18, No. 6, 2010, pp. 655–665. doi:10.1007/s10934-010-9423-z.

[27] Despois, J., and Mortensen, A., "Permeability of open-pore microcellular materials," *Acta Materialia*, Vol. 53, No. 5, 2005, pp. 1381–1388. doi:10.1016/j.actamat.2004.11.031.

[28] Bonnet, J., Topin, F., and Tadrist, L., "Flow Laws in Metal Foams: Compressibility and Pore Size Effects," *Transport in Porous Media*, Vol. 73, No. 2, 2007, pp. 233–254. doi:10.1007/s11242-007-9169-5.

[29] Geyer, T., Sarradj, E., and Fritzsche, C., "Porous Airfoils: Noise Reduction and Boundary Layer Effects," *15th AIAA/CEAS Aeroacoustics Conference (30th AIAA Aeroacoustics Conference)*, American Institute of Aeronautics and Astronautics, 2009. doi:10.2514/6.2009-3392.

[30] Geyer, T., Sarradj, E., and Fritzche, C., "Measurement Of The Noise Generation At The Trailing Edge Of Porous Airfoils," *Experiments In Fluids*, Vol. 48, No. 291, 2010. doi:10.1007/s00348-009-0739-x.

[31] Luesutthiviboon, S., Malgoezar, A., Snellen, M., Sijtsma, P., and Simons, D., "Improving Source Discrimination Performance by Using an Optimized Acoustic Array and Adaptive High-Resolution Clean-SC Beamforming," *7th Berlin Beamforming Conference*, 2018, pp. 1–27.

[32] Sijtsma, P., Merino-Martinez, R., Malgoezar, A. M., and Snellen, M., "High-resolution CLEAN-SC: Theory and experimental validation," *International Journal of Aeroacoustics*, Vol. 16, No. 4-5, 2017, pp. 274–298. doi:10.1177/1475472x17713034.

[33] Rayleigh, L., "Investigations in optics, with special reference to the spectroscope," *Philosophical Magazine Series 5*, Vol. 8, No. 49, 1879, pp. 261–274. doi:10.1080/14786447908639684.

[34] Merino-Martínez, R., Snellen, M., and Simons, D. G., "Functional Beamforming Applied to Imaging of Flyover Noise on Landing Aircraft," *Journal of Aircraft*, Vol. 53, No. 6, 2016, pp. 1830–1843. doi:10.2514/1.c033691.

[35] Mueller, T. J., *Aeroacoustic measurements*, Berlin New York Springer, 2002. doi:10.1007/978-3-662-05058-3.

[36] Arce León, C., Merino-Martínez, R., Ragni, D., Avallone, F., and Snellen, M., "Boundary layer characterization and acoustic measurements of flow-aligned trailing edge serrations," *Experiments in Fluids*, Vol. 57, No. 12, 2016, p. 182. doi:10.1007/s00348-016-2272-z.

[37] Sarradj, E., Herold, G., Sijtsma, P., Martinez, R. M., Geyer, T. F., Bahr, C. J., Porteous, R., Moreau, D., and Doolan, C. J., "A Microphone Array Method Benchmarking Exercise using Synthesized Input Data," *23rd AIAA/CEAS Aeroacoustics Conference. Denver, Colorado.*, 2017. doi:10.2514/6.2017-3719.

[38] Merino-Martínez, R., van der Velden, W., Avallone, F., and Ragni, D., "Acoustic measurements of a DU96-W-180 airfoil with flow-misaligned serrations at a high Reynolds number in a closed-section wind tunnel," *7th International Conference on Wind Turbine Noise: Rotterdam*, 2017, pp. 1–14.

[39] Merino-Martínez, R., Sijtsma, P., and Snellen, M., "Inverse Integration Method for Distributed Sound Sources," *7th Berlin Beamforming Conference*, 2018, pp. 1–21.

[40] Raffel, M., Willert, C. E., and Kompenhans, J., *Particle Image Velocimetry*, Springer Berlin Heidelberg, 1998. doi: 10.1007/978-3-662-03637-2.

[41] Scarano, F., and Riethmuller, M., "Advances in Iterative multigrid PIV Image Processing," *Experiments in Fluids*, Vol. 29, 2000, pp. 51–60. doi:10.1007/s003480070007.

[42] Scarano, F., "Iterative image deformation methods in PIV," *Measurement Science and Technology*, Vol. 13, No. 1, 2001, pp. R1–R19. doi:10.1088/0957-0233/13/1/201.

[43] Westerweel, J., and Scarano, F., "Universal outlier detection for PIV data," *Experiments in Fluids*, Vol. 39, No. 6, 2005, pp. 1096–1100. doi:10.1007/s00348-005-0016-6.

[44] Brandt, A., *Noise and Vibration Analysis: Signal Analysis and Experimental Procedures*, John Wiley & Sons, ltd, 2011. doi:10.1002/9780470978160.

[45] Westerweel, J., "Fundamentals of digital particle image velocimetry," *Measurement Science and Technology*, Vol. 8, No. 12, 1997, pp. 1379–1392. doi:10.1088/0957-0233/8/12/002.

[46] Melling, A., "Tracer particles and seeding for particle image velocimetry," *Measurement Science and Technology*, Vol. 8, No. 12, 1997, pp. 1406–1416. doi:10.1088/0957-0233/8/12/005.

[47] Moffat, R. J., "Describing the uncertainties in experimental results," *Experimental Thermal and Fluid Science*, Vol. 1, No. 1, 1988, pp. 3–17. doi:10.1016/0894-1777(88)90043-x.

[48] Wieneke, B., "PIV uncertainty quantification from correlation statistics," *Measurement Science and Technology*, Vol. 26, No. 7, 2015, p. 074002. doi:10.1088/0957-0233/26/7/074002.

[49] Spalart, P. R., and Watmuff, J. H., "Experimental and numerical study of a turbulent boundary layer with pressure gradients," *Journal of Fluid Mechanics*, Vol. 249, No. 1, 1993, p. 337. doi:10.1017/s002211209300120x.

[50] Moßner, M., and Radespiel, R., "Flow simulations over porous media – Comparisons with experiments," *Computers & Fluids*, Vol. 154, 2017, pp. 358–370. doi:10.1016/j.compfluid.2017.03.002.

[51] Krogstad, P., Antonia, R. A., and Browne, L. W. B., "Comparison between rough- and smooth-wall turbulent boundary layers," *Journal of Fluid Mechanics*, Vol. 245, No. 1, 1992, p. 599. doi:10.1017/s0022112092000594.

[52] Flack, K. A., and Schultz, M. P., "Roughness effects on wall-bounded turbulent flows," *Physics of Fluids*, Vol. 26, No. 10, 2014, p. 101305. doi:10.1063/1.4896280.

[53] Hutchins, N., Monty, J., Nugroho, B., Ganapathisubramani, B., and Utama, I., "Turbulent boundary layers developing over rough surfaces: from the laboratory to full-scale systems." *20th Australasian Fluid Mechanics Conference*, 2016, pp. 1–8.

[54] Williams, J. E. F., and Hall, L. H., "Aerodynamic sound generation by turbulent flow in the vicinity of a scattering half plane," *Journal of Fluid Mechanics*, Vol. 40, No. 04, 1970, p. 657. doi:10.1017/s0022112070000368.

[55] Ali, S. A. S., Azarpeyvand, M., and da Silva, C. R. I., "Experimental Study of Porous Treatment for Aerodynamic and Aeroacoustic Purposes," *23rd AIAA/CEAS Aeroacoustics Conference*, American Institute of Aeronautics and Astronautics, 2017. doi:10.2514/6.2017-3358.

[56] Kolmogorov, A., "The Local Structure of Turbulence in Incompressible Viscous Fluid for Very Large Reynolds Numbers," *Doklady Akademiia Nauk SSSR*, Vol. 30, 1941, pp. 301–305.

[57] Ghaemi, S., and Scarano, F., "Turbulent structure of high-amplitude pressure peaks within the turbulent boundary layer," *Journal of Fluid Mechanics*, Vol. 735, 2013, pp. 381–426. doi:10.1017/jfm.2013.501.